# Planar Gamma Camera Imaging and Quantitation of Yttrium-90 Bremsstrahlung

Sui Shen, Gerald L. DeNardo, Aina Yuan, Diane A. DeNardo and Sally J. DeNardo

*University of California at Davis, School of Medicine, Sacramento, California*

Yttrium-90 is a promising radionuclide for radioimmunotherapy of cancer because of its energetic beta emissions. Therapeutic management requires quantitative imaging to assess the pharmacokinetics and radiation dosimetry of the $^{90}$Y-labeled antibody. Conventional gamma photon imaging methods cannot be easily applied to imaging of $^{90}$Y-bremsstrahlung because of its continuous energy spectrum. **Methods:** The sensitivity, resolution and source-to-background signal ratio (S/B) of the detector system for $^{90}$Y-bremsstrahlung were investigated for various collimators and energy windows in order to determine optimum conditions for quantitative imaging. After these conditions were determined, the accuracy of quantitation of $^{90}$Y activity in an Alderson abdominal phantom was examined. **Results:** When the energy-window width was increased, the benefit of increased sensitivity outweighed degradation in resolution and S/B ratio until the manufacturer's energy specifications for the collimator were exceeded. Using the same energy window, we improved resolution and S/B for the medium-energy (ME) collimator when compared to the low-energy, all-purpose (LEAP) collimator, and there was little additional improvement using the high-energy (HE) collimator. Camera sensitivity under tissue equivalent conditions was 4.2 times greater for the LEAP and 1.7 times greater for the ME collimators when compared to the HE collimator. Thus, the best, most practical selections were found to be the ME collimator and an energy window of 55–285 keV. When we used these optimal conditions for image acquisition, the estimation of $^{90}$Y activity in organs and tumors was within 15% of the true activities. **Conclusions:** The results of this study suggest that reasonable accuracy can be achieved in clinical radioimmunotherapy using $^{90}$Y-bremsstrahlung quantitation.

**Key Words:** bremsstrahlung imaging; yttrium-90; radioimmunotherapy; radiation dosimetry; antibody

**J Nucl Med 1994; 35:1381–1389**

Yttrium-90, a pure beta emitter, has attracted considerable attention as a therapeutic radionuclide because its long-range beta emissions mitigate the problem of tumor penetration, and its lack of gamma emissions lessen radiation safety concerns (*1,2*). The absence of gamma emissions from $^{90}$Y for imaging has led to the use of $^{111}$In, a radionuclide with analogous chemical properties and good imaging photons, as a tracer for $^{90}$Y pharmacokinetics and radiation dosimetry. Although the chemical properties of $^{90}$Y and $^{111}$In are similar, they are not identical; it has become apparent that $^{111}$In may not predict $^{90}$Y behavior with complete accuracy, even when state-of-the-art chelates are used to prepare the immunoconjugates (*3*). Discrepancy in biological behavior has led to unanticipated hematopoietic toxicity from $^{90}$Y in clinical trials of radioimmunotherapy (*4*). Yttrium-90 has secondary photon emissions but these bremsstrahlung radiations have a broad spectrum of energies and are not abundant, so choices of collimation and energy window are complex. Efforts to obtain radiation dosimetric data by quantitative imaging of the bremsstrahlung from pure beta emitting radionuclides have been recently reported (*5,6*). The purpose of this publication is to report the results from a systematic, empirical evaluation of collimator, spectral window and attenuation correction for quantitative imaging of $^{90}$Y-bremsstrahlung, and the accuracy that can be obtained when optimal techniques are used in a simulated abdominal phantom containing organs and tumors.

## MATERIALS AND METHODS

### Detector System and Collimation

Two gamma cameras, a ZLC-7500 Orbiter (Siemens Medical Systems, Inc., Des Plaines, IL) with a circular (39-cm diameter) NaI(Tl) crystal and a Dual Detector Bodyscan (Siemens Medical Systems, Inc., Des Plaines, IL) with a rectangular (61 cm × 39 cm) NaI(Tl) crystal were employed to acquire $^{90}$Y data. All three crystals are 0.95-cm thick. Each camera was fitted with either a LEAP, ME or HE parallel-hole collimator and was interfaced to a Siemens Micro/Maxdelta (Des Plaines, IL) computer system. The design parameters of the collimators for each camera are provided in Table 1. Both cameras were used to measure the percentage of counts in the field of view (% FOV) and source-to-background ratio (S/B). The system resolution of the two cameras was comparable according to manufacturer's specifications; the difference in FWHM was 4% for the LEAP collimator and $^{99m}$Tc, 3% for the ME collimator and $^{67}$Ga, and 2% for the HE collimator and $^{131}$I. The Orbiter camera system was used to detect changes in bremsstrahlung spectra and resolution, and the dual-detector Bodyscan camera system was used for the phantom studies. Images were acquired in 128 × 128 word-mode matrix. The average counts of the source object were greater than 270 counts/pixel, providing less than 6% statistical error. Using a standard geometry, a $^{90}$Y sample dispersed uniformly in a 10-ml plastic vial was

Received Oct. 6, 1993; revision accepted Mar. 9, 1994.

For correspondence or reprints contact: Sui Shen, PhD, 1508 Alhambra Blvd., Rm. 214, Sacramento, CA 95816.

**TABLE 1**
Manufacturer's Specifications for Septal Penetration, Sensitivity* and Energy Windows Investigated for Yttrium-90 Imaging

| Collimator | 5% septal penetration | Relative sensitivity† | $^{90}$Y energy windows |
|---|---|---|---|
| Low energy | <160 keV | 1.00 | 68–83 keV (75 keV ± 10%) |
| | | | 50–150 keV (100 keV ± 49.5%) |
| | | | 144–176 keV (160 keV ± 10%) |
| Medium energy | <295 keV | 0.80 | 68–83 keV (75 keV ± 10%) |
| | | | 55–285 keV (75 keV ± 27% & 190 keV ± 49.5%) |
| | | | 113–138 keV (125 keV ± 10%) |
| | | | 84–156 keV (125 keV ± 25%) |
| | | | 63–186 keV (125 keV ± 49.5%) |
| High energy | <395 keV | 0.42 | 68–83 keV (75 keV ± 10%) |
| | | | 55–285 keV (75 keV ± 27% & 190 keV ± 49.5%) |
| | | | 113–138 keV (125 keV ± 10%) |
| | | | 84–156 keV (125 keV ± 25%) |
| | | | 63–188 keV (125 keV ± 49.5%) |

*Septal penetration and relative sensitivity are the same for collimators on the Bodyscan and Orbiter camera systems.
†Sensitivity relative to the LEAP collimator for $^{99m}$Tc using a 140 keV ± 10% window.

assayed in a dose calibrator (Capintech CRC-12, Ramsey, NJ) at a setting recommended by the manufacturer. A better than 1% accuracy was achieved for all source concentrations using an automatic pipetting device (Pipetman specifications, Rainin, Woburn, MA).

### Bremsstrahlung Energy Window

*Sensitivity and Resolution.* The effects of change in energy window and collimation on the $^{90}$Y spectra and detector-system parameters were investigated. The lowest energy level detectable by the camera systems was 50 keV. The upper level of the energy windows was limited to the energy at which 5% penetration would occur according to the manufacturer's specifications for the collimator (Table 1). The complete bremsstrahlung energy spectra with and without collimators were obtained using an 85.1 MBq (2.3 mCi) $^{90}$Y point source (volume, 6.3 mm$^3$) made of lucite (thickness, 5 mm) and residing on a cardboard box at a distance of 200 cm (5 FOVs) from the detector. Integration of the energy spectra within the pulse-height analyzer of the system (50–510 keV) was performed to determine the percent of photons within the energy window relevant to each collimator.

Energy windows were varied to determine sensitivity, intrinsic and system resolution, and S/B of the detector system. The widest energy window that could be evaluated was 55–285 keV because of the design of the energy selection system. An 85.1 MBq (2.3 mCi) $^{90}$Y point source was placed in the center of the FOV in air at 6 cm and in lucite at a depth of 9 cm from the detector to simulate scattering conditions found in tissue, and to determine camera sensitivity and S/B with and without scatter. The intrinsic resolution of the camera for $^{90}$Y was examined using a 10-ml source 200 cm from the detector and a lead-bar phantom adjacent to the crystal. The system resolution of the camera for $^{90}$Y, full-width at half-maximum (FWHM) and full-width at tenth-maximum (FWTM) of the point-spread function (PSF), was determined for various energy windows using a point source that was placed behind various thicknesses (1.8–9.0 cm) of scattering medium (lucite), the edge of which was 5 cm from the detector. Lucite was used because it closely simulated the density of tissue (0.944 g/cc).

*Source-to-Background/Scatter.* Here, S/B was defined by:

$$S/B = \frac{\text{source count rate} - \text{background count rate}}{\text{background count rate}}. \quad \text{Eq. 1}$$

The effect of energy-window width on S/B was investigated using the ME and HE collimators. Window widths of 20%, 50% and 99% centered at 125 keV (113–138 keV, 84–156 keV and 63–186 keV) were examined using an $^{90}$Y source with activity of 1810 MBq (49 mCi) in 10 ml in air. Source-to-background ratios of the images were also compared using LEAP (50–150 keV), ME (55–285 keV) and HE (55–285 keV) collimator with source in air and in scattered medium of lucite.

The counts-in-source regions-of-interest (ROIs) of different sizes as a percentage of the total counts in the FOV were used to evaluate the bremsstrahlung scattering for each collimator. Greater % FOV counts in the ROI indicates less photon scattering. A ROI was drawn for a 10-ml source placed in the center of the FOV so that the linear number of pixels in the ROI corresponded to the known source diameter. The background ROI was defined near the edge of the FOV. The counts in the source ROI were expressed as % FOV in order to evaluate the effect of scatter. The % FOV was determined by:

$$\%\ \text{FOV} = \frac{\text{counts in the source ROI}}{\text{total counts in the field-of-view}}. \quad \text{Eq. 2}$$

*Optimal Imaging Conditions.* Detection system parameters (sensitivity, resolution, S/B and % FOV) of LEAP, ME and HE collimators were compared. The optimal selections for collimator and energy window for bremsstrahlung imaging under clinical conditions were determined from a practical compromise of these parameters. The optimal selections of energy window and collimator were then applied to quantitative studies of an abdominal phantom containing organs and tumors.

### Phantom Measurements

*Phantom.* The abdominal phantom (Alderson Research Laboratories, Inc., Stamford, CT) was a plastic cavity containing a liver, spleen, 2-cm and 4-cm spherical tumors. The positions of the organs and tumors are illustrated in a schematic cross-sec-

tional view of the phantom (Fig. 1). The organs and tumors were uniformly filled with a measured amount of $^{90}Y$ to simulate the organ concentrations observed in patients after a therapy dose. The concentrations in the liver, spleen, 4-cm tumor and 2-cm tumor were 666 kBq/ml (1.8 μCi/ml), 118 kBq/ml (3.2 μCi/ml), 200 kBq/ml (5.4 μCi/ml) and 440 kBq/ml (11.9 μCi/ml), respectively. These concentrations correspond to 18% (0.012 %/ml), 3.1% (0.021 %/ml), 1.2% (0.036 %/ml) and 0.3% (0.071 %/ml) uptake of a dose of 555 MBq (15 mCi) in a patient. A $^{90}Y$ concentration of 5.92 kBq/ml (0.16 μCi/ml) corresponding to 8.0% (0.0011 %/ml) was added to the background volume of the phantom to simulate the liver S/B of five that has been typically observed in our $^{90}Y$ patient studies (*2*).

*Image Acquisition.* Phantom images were acquired in a 128 × 128 word-mode matrix on the Bodyscan camera. The anterior and posterior surfaces of the phantom were 5 cm from the upper and lower detectors. Based upon the preliminary studies, a ME collimator with an energy window of 55–285 keV was selected to provide optimum sensitivity and resolution. A 10-ml source of 14.8 MBq (400 μCi) $^{90}Y$ was placed directly on the collimator to determine the system calibration factor in counts/kBq/second. One million counts were recorded in about 500 sec for each image of the phantom.

*Linear Attenuation Coefficient (μ).* The μ value from a narrow beam was measured using a cylindrical lead collimator that was lined with a plastic tube (inner diameter of 3 mm, 1-cm thick) to hold the 148-MBq (4 mCi) $^{90}Y$ sample. The distance between the $^{90}Y$ source and the opening of the source collimator was 15 cm and the size of the outlet was 5 mm to simulate narrow-beam geometry. Various thicknesses of lucite (1.8–9.0 cm) between the beam source and the camera were used as scattering medium.

An effective μ value was measured using transmission fraction (TF) data from a 5-cm spherical source. This effective μ value was an integrated value obtained by exponential-curve fitting of TF data for the source at different depths in water. The TF was determined from the formula:

$$TF = C/C_0, \qquad \text{Eq. 3}$$

where C = cts/sec from the source at depth (d) in water and $C_0$ = cts/sec from the source in air at the same distance from the collimator as that in water. Circular ROIs of 5 cm (actual source size) and 10 cm (twice the source size) in diameter were used to examine the influence of ROI size on μ value.

*Image Quantitation.* The effective point-source method (*7,8*) was used to determine spleen and 2-cm tumor activity because these objects were only seen in one view:

$$A = Ie^{\mu d}/c, \qquad \text{Eq. 4}$$

where A = organ or tumor activity (kBq), I = cts/sec within the ROI, μ = effective linear attenuation coefficient measured using the 5-cm spherical source in water, d = effective organ or tumor depth and c = system calibration factor (cts/kBq/sec). The geometric-mean method (*7–10*) was employed for image quantitation of the liver and 4-cm tumor that were seen in anterior and posterior views:

$$A = (I_a I_p)^{1/2} e^{\mu T/2} f/c, \qquad \text{Eq. 5}$$

where A = organ or tumor activity (kBq), $I_a$ = cts/sec in the anterior view, $I_p$ = counts/second in the posterior view, μ = the effective linear attenuation coefficient ($cm^{-1}$) for the body, T = the thickness (cm) of the phantom in the area of the ROI, f = self-attenuation correction factor and c = system calibration factor (cts/kBq/sec). The attenuation correction factor (ACF) defined as $e^{\mu T/2}$ was determined from a transmission image of the abdominal phantom for a large object like the liver. Transmission scan images were obtained using a rod source (acrylic tube of 1.5-cm inner diameter, 5-mm thickness) containing 92.5 MBq (2.5 mCi) of uniformly dispersed $^{90}Y$. The ACF was derived using the equation:

$$ACF = (N_{(0)}/N_{(T)})^{1/2}, \qquad \text{Eq. 6}$$

where $N_{(0)}$ = counts in the ROI in the absence of the abdominal phantom and $N_{(T)}$ = counts in the ROI in the presence of the abdominal phantom. For the small 4-cm tumor, $e^{\mu T/2}$ was calculated by the effective linear attenuation coefficient, μ, measured from a 5-cm spherical source and effective depths of the tumor in water. The ROIs for the organs and tumors were determined by the known size of these objects and corresponded to a 40% threshold of maximal pixel counts for the liver and 60% for the spleen and tumors. In clinical studies, ROIs for organs and tumors can be determined using x-ray CT or MRI. Background ROIs were selected with the same body thickness as that of the overlapping background volume of the organs or tumors to perform background subtraction.

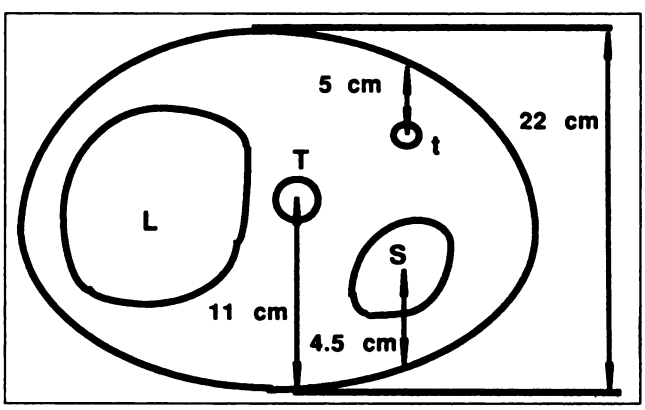


**FIGURE 1.** A transverse cross-sectional schematic of the abdominal phantom showing the liver (L) and spleen (S). A 4-cm tumor (T) was located in the center of the phantom and a 2-cm tumor (t) was located 5 cm from the anterior surface.

## RESULTS

### Bremsstrahlung Energy Window

The continuous bremsstrahlung spectrum in the absence of a collimator is shown in Figure 2. In the absence of a collimator, the percentage of all recorded photons that were detected within energy windows of 50–150 keV, 50–290 keV and 50–390 keV (corresponding to recommended energy ranges for LEAP, ME and HE collimators, respectively) were 54%, 80% and 86%, respectively (Table 2). Although more photons were detected within wider windows with each collimator, as well as without a collimator, the differences between the ME and HE collimator were quite small (Table 2). A characteristic x-ray peak at approximately 75 keV was superimposed on the continuous bremsstrahlung spectrum when lead collimators were

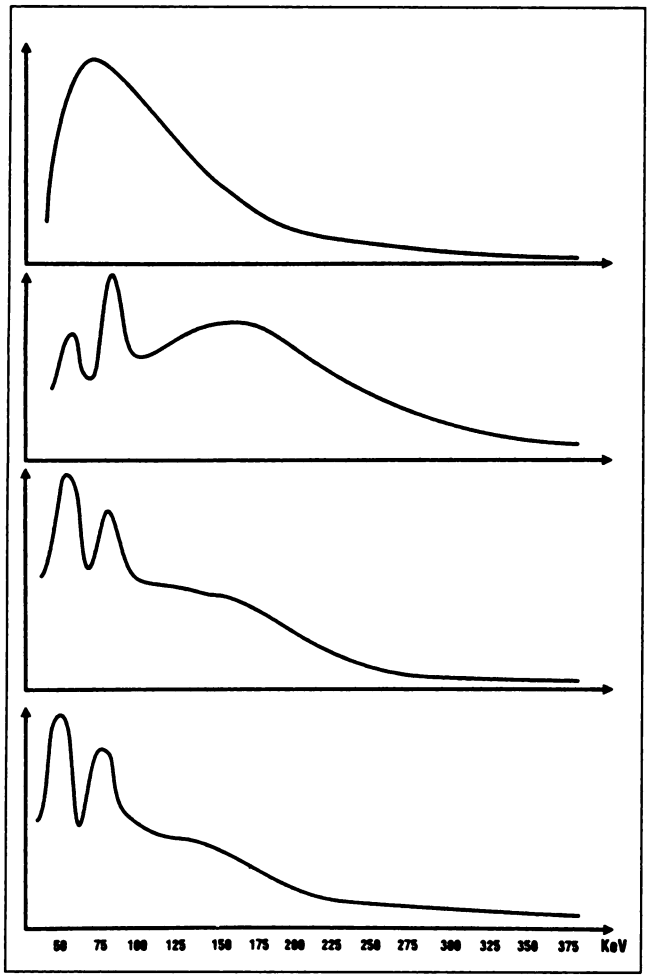


**FIGURE 2.** Bremsstrahlung spectra without (top) and with (second, third and fourth graphs from top) lead collimators. The spectrum was continuous without the collimator in place (top). The spectra revealed a characteristic x-ray peak at 75 keV when using the low-energy collimator (second from top), the medium-energy collimator (third from top), and the high-energy collimator (fourth from top) and septal penetration at about 160 keV (LEAP collimator).

mounted (Figure 2). The rise in the spectrum at approximately 160 keV reflected penetration of the septa of the collimators by higher-energy bremsstrahlung photons (Figure 2). Septal penetration was greatest for the LEAP collimator (Figure 2). Considering the appropriate energy window and collimation, we found that the percentage of all recorded photons that were detected within energy windows of 50–150 keV with the LEAP, or 50–290 keV with the ME or 50–390 keV with the HE collimator were 30%, 68% and 75%, respectively (Table 2). Using the energy windows recommended by the manufacturer for each collimator, the percent of all photons recorded in the recommended windows was almost the same for the ME and the HE collimators.

*Sensitivity and Resolution.* An increase in sensitivity for each collimator occurred when energy-window width was increased (Table 3). The sensitivities were greatest for the LEAP collimator using the 50–150 keV energy window as expected. Intrinsic images resolved 3-mm bars of a bar phantom, even with greater energy-window width. There were no detectable differences in system resolution with changes in energy-window center or width when the window center and width were within the manufacturer's specifications for the respective collimator (Table 3). Resolution decreased when energies beyond the manufacturer's specifications for the collimators were included in the energy window, for example FWHM was 30 mm for a 144–176 keV energy window using the LEAP collimator. System resolution was substantially better for the ME collimator when compared to the LEAP collimator, whereas resolution of the ME collimator was comparable to that of the HE collimator for equivalent energy windows and lucite thicknesses (Table 3).

*Source to Background/Scatter.* Using a HE collimator, S/B decreased as the energy-window width was increased (Fig. 3). This effect was less appreciable for the ME collimator. Source-to-background ratios of the ME and HE collimators were similar when wider window widths consistent with clinical conditions were used. For a fixed window width of 99% centered at 125 keV, the S/B increased as source activity increased for the ME and HE collimator, but this improvement was not apparent for the HE collimator until 10 mCi of $^{90}Y$ was used (Fig. 4). This was attributable to counts from natural radiation registered in the wide-energy window.

The % FOV counts in the actual ROI (2.5 cm) or in the actual ROI × 2 (5 cm) were much less for the LEAP collimator than for the ME collimator but only slightly less for the ME than for the HE collimator (Table 4). Scattering manifested by greater % FOV counts in the ROI × 2 than in the actual ROI was greater for the LEAP collimator than for the ME or the HE collimators. Scattering was similar for the ME and HE collimators.

*Optimal Imaging Conditions.* Sensitivity in air was three times greater for the LEAP than for the ME or HE collimator, and the sensitivity was 1.7 times greater for the ME than for the HE collimator (Table 5). For the same energy window, system resolution with scatter was almost equal for the ME and HE collimators and was three times better than the LEAP collimator. The relative scatter effects, as depicted by % FOV counts occurring outside of the ROI, were comparable for ME and HE collimators, and were

**TABLE 2**
**Percentage of Total Spectral Photons Detected within Energy Windows Relevant to Imaging Yttrium-90 Bremsstrahlung with Low-, Medium- and High-Energy Collimators**

| | Total spectral photons within energy window (%) | | |
|---|---|---|---|
| Collimator | 50–150 keV | 50–290 keV | 50–390 keV |
| None | 54 | 80 | 86 |
| Low-energy | 30 | 64 | 77 |
| Medium-energy | 39 | 68 | 75 |
| High-energy | 40 | 67 | 75 |

**TABLE 3**
System Resolution and Sensitivity for Yttrium-90 with Various Collimators, Energy Windows and Thicknesses of Scattering Medium (Lucite)

| Collimator | Energy window (keV) | Sensitivity in air (cps/MBq) | Lucite thickness (cm) | System resolution FWHM (mm) | System resolution FWTM (mm) |
|---|---|---|---|---|---|
| Low-energy | 68–83 | 8.38 | 1.8 | 15 | 40 |
| | | | 3.6 | 16 | 45 |
| | | | 9.0 | 20 | 70 |
| | 50–150 | 40.0 | 1.8 | 15 | 40 |
| | | | 3.6 | 16 | 45 |
| | | | 9.0 | 20 | 90 |
| Medium-energy | 68–83 | 1.89 | 1.8 | 12.5 | 24 |
| | | | 3.6 | 13 | 24 |
| | | | 9.0 | 16.5 | 32 |
| | 55–285 | 11.6 | 1.8 | 12.5 | 24 |
| | | | 3.6 | 13 | 26 |
| | | | 9.0 | 16.5 | 32 |
| High-energy | 68–83 | 1.08* | 1.8 | 12.5 | 24 |
| | 55–285 | 6.75 | 1.8 | 12.5 | 24 |
| | | | 3.6 | 13 | 26 |
| | | | 9.0 | 16 | 30 |

*Only the 1.8-cm thickness of lucite was measured for the high-energy collimator because of the low sensitivity for this narrow energy-window width.

less than those for the LEAP collimator. Signal-to-background ratios for the HE and ME collimators were three times greater than that for the LEAP collimator. The degradation effect on resolution, S/B and % FOV was small in comparison to the increase in sensitivity when energy-window width was increased. Therefore, the ME collimator with a wide-energy window (55–285 keV) was the optimal selection for achieving a clinical compromise between sensitivity and resolution.

## Phantom Quantitation

*Linear Attenuation Coefficient.* An exponential curve fit was applied to the TF data that were obtained using a collimated beam source and scattering medium (lucite) to obtain the average linear attenuation coefficient for $^{90}Y$. Window width and collimation had little effect on the average linear attenuation coefficient (correlation of regression fitting > 0.99) (Table 6). The TF data for measured counts within ROIs at different depths of water are shown

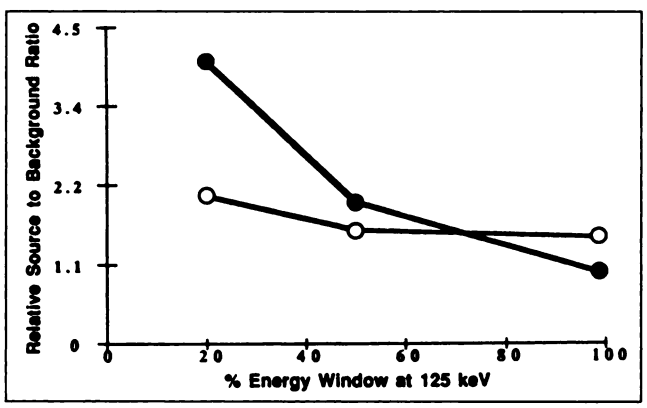


**FIGURE 3.** Source-to-background signal ratios for medium (○-○) and high-energy collimators (●-●) using 20%, 50%, or 99% energy window widths centered at 125 keV. Source-to-background signal ratios are expressed relative to those obtained using the 99% energy window and the high-energy collimator. Source-to-background signal ratios decreased as the energy window width increased.

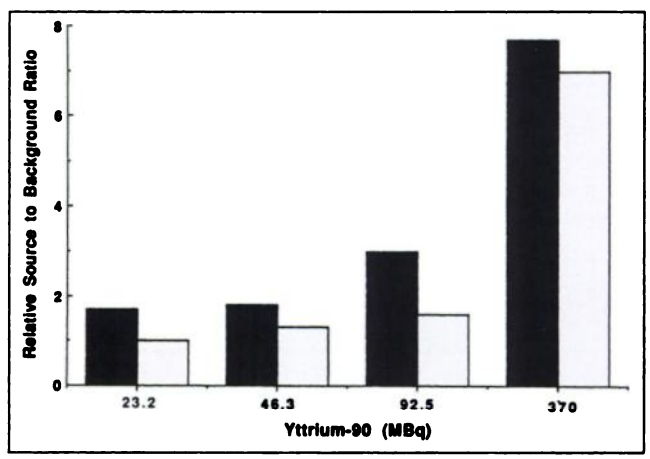


**FIGURE 4.** Source-to-background signal ratios for 23 (0.63), 46 (1.3), 93 (2.5), or 370 (10) MBq (mCi) of $^{90}Y$ using the medium-energy (■) and high-energy (□) collimator relative to the high-energy collimator and 23 MBq (0.63 mCi) of $^{90}Y$. Source to background signal ratios increased as $^{90}Y$ activity increased for both collimators even when using a 99% energy window centered at 125 keV.

**TABLE 4**
Effect of Bremsstrahlung Scattering as Percentage of Total Image Counts in Yttrium-90 Source ROIs Corresponding to the Actual (2.5 cm) and Twice the Actual (5 cm) Source Size

| Collimator | Energy window (keV) | Lucite thickness (cm) | % of FOV Counts in the ROI | |
|---|---|---|---|---|
| | | | 2.5-cm ROI | 5-cm ROI |
| Low-energy | 68–82 | 1.8 | 18 | 30 |
| | | 3.6 | 17 | 29 |
| | | 9.0 | 15 | 23 |
| | 50–150 | 1.8 | 18 | 27 |
| | | 3.6 | 15 | 24 |
| | | 9.0 | 11 | 20 |
| Medium-energy | 55–285 | 1.8 | 38 | 45 |
| | | 3.6 | 31 | 38 |
| | | 9.0 | 23 | 35 |
| High-energy | 55–285 | 1.8 | 42 | 50 |
| | | 3.6 | 37 | 47 |
| | | 9.0 | 26 | 40 |

in Figure 5 for the effective attenuation coefficient ($\mu$) determined from the 5-cm spherical source. The $\mu$ was measured to be 0.131 for the ROI of 5-cm diameter and 0.117 for the ROI of 10-cm diameter. The correlation coefficient was 0.99 for each of the ROIs. This suggested that a single $\mu$ value can be used for attenuation correction even when multi-energy bremsstrahlung photons were acquired in a broad-energy window.

We used the geometric-mean method for the liver and 4-cm tumor, and the effective point-source method for the spleen and 2-cm tumor to quantify activity. The ACF for the liver and 4-cm tumor measured from a rod transmission image was 1.30 and 1.40, respectively. For objects only seen from a single view (spleen, 2-cm tumor), attenuation was corrected by $e^{\mu d}$ using a $\mu$ value of 0.131 $cm^{-1}$.

*Organ or tumor quantitation.* Activity of organs and tumors in the phantom was underestimated in all instances. Organ and tumor ROIs were drawn according to known phantom sizes. Accurate quantitation in organs and tumors depends on correct compensation of photon attenuation, scattering and activity in the background. The results of $^{90}Y$ estimation for each organ and tumor are shown in Table 7. The estimation of liver activity was approximately twice that of the actual activity when photon attenuation was corrected using a $\mu$ value of 0.131 $cm^{-1}$ (+103% error). The estimation error was considerably less for the liver when corrected with the ACF from the transmission image. There was an activity underestimation of about 70% for the 4-cm tumor when photon attenuation was corrected using the ACF measured from transmission imaging. These results clearly indicate the significant effect of broad-beam geometry on the transmission fraction in bremsstrahlung imaging. The large amount of scattering from the broad beam of the transmission rod was suitable for ACF determination of a large source like the liver, though not suitable for a small object like a tumor. More accurate estimation was achieved when the liver attenuation was corrected with the ACF and the 4-cm tumor attenuation was corrected using the $\mu$ value.

Proper selection of the background ROI was important for performing background subtraction. For example, when the background ROI was approximately 10 cm away from the spleen and 2-cm tumor towards the lateral portion of the phantom (a thinner area with less attenuation), overestimation of $^{90}Y$ was 47% for the spleen and 138% for the 2-cm tumor. When the background ROI was selected 2-cm inferior to the spleen or 2-cm tumor (an area of equal thickness of overlapping background volume), the estimations were within 15% for the spleen and 2-cm tumor. Estimation accuracy for a small source object (2-cm tumor) was more sensitive to background ROI selection than for a larger object (spleen).

## DISCUSSION

Pure, beta-emitting radionuclides ($^{32}P$, $^{90}S$, $^{90}Y$) have been widely used for therapy to deliver an intense, localized radiation dose to the target tissue (*11–19*). The advent of $^{90}Y$-labeled monoclonal antibodies has made delivery of more uniform radiation doses to solid tumors possible be-

**TABLE 5**
System Detection Parameters for Yttrium-90 Using Various Collimators and Energy Windows

| Collimator | Energy window (keV) | Sensitivity* | | Resolution* | | Source-to-Background* | |
|---|---|---|---|---|---|---|---|
| | | Air | Lucite | FWTM (mm) | % FOV | Air | Lucite |
| Low-energy | 50–150** | 1.00 | 1.00 | 90 | 1.0 | 1.0 | 1.0 |
| Medium-energy† | 55–285 | 0.29 | 0.40 | 32 | 2.1 | 3.2 | 3.6 |
| High-energy | 55–285 | 0.17 | 0.24 | 30 | 2.4 | 3.5 | 3.9 |

*Sensitivity, resolution and source-to-background signal ratio for the source in air and behind 9-cm lucite. Values for sensitivity, % FOV and source-to-background signal ratio normalized to that of the low-energy collimator, 50–150 keV.

**An energy maximum of 150 keV was used for the low-energy collimator in order to stay within the manufacturer's specifications for energy absorption.

†The medium energy collimator with an energy window of 55–285 keV provided the best clinical compromise between sensitivity and resolution.

cause the highly energetic beta emissions of $^{90}Y$ overcome problems of tumor penetration (*1,2*). While a substantial increase in radiation dose to tumor can be achieved with $^{90}Y$-labeled antibodies, evaluation of radiation dosimetry is difficult because of the lack of primary photon emissions. Indium-111 has been used as a tracer to identify the distribution of $^{90}Y$-labeled antibodies but has not proven entirely satisfactory for predicting $^{90}Y$ myelotoxicity (*2*). Although better chelates for $^{90}Y$ have become available and further improvements are likely, some of those currently used permit transfer of $^{90}Y$ to the skeleton leading to myelotoxicity (*3*). Even when chelates capable of tightly binding $^{90}Y$, such as macrocyclic DOTA, are used (*20*), there is a need to determine radiation dosimetry and corroborate absence of transfer of $^{90}Y$ using imaging methods. Additionally, $^{111}In$ and $^{90}Y$ radiopharmaceuticals are often formulated at the clinical site using kits. In this circumstance, or even if the radiopharmaceutical was formulated centrally, there is opportunity for variation in individual preparations so they contain less tightly bound $^{90}Y$ (or $^{111}In$). Therefore, $^{90}Y$ imaging is relevant to the management of a patient's therapeutic plan because the plan should be modified if there has been instability of the radioimmunoconjugate.

Until approximately a decade ago, $^{90}Y$ imaging was limited to gross definition of the degree of uniformity of distribution of $^{90}Y$-labeled radiopharmaceuticals in spaces such as the abdominal cavity and joints after local injections (*1,21*). Improvements in imaging beta emitters such as $^{90}Y$ have led to more definitive imaging (*22–25*). Recently, attention has been given to quantitative imaging of bremsstrahlung events in order to obtain radiation dose estimates. Preparatory to studies in patients, spheres in water were quantitated for $^{89}Sr$ activity by Siegel et al. (*5*) and for $^{32}P$ activity by Clarke et al. (*6*). Siegel et al. (*5*) used a ME collimator and 53–148-keV window for imaging of $^{89}Sr$, whereas Clarke et al. (*6*) used a long-bore HE collimator and 57–285 keV window attempting to minimize septal penetration for imaging of $^{32}P$. Balachandran et al. (*24*) used a LEAP collimator and 40–150-keV window to achieve greater sensitivity for $^{32}P$ imaging.

The spatial and energy dependence of bremsstrahlung production causes an inherent limitation in spatial resolution for bremsstrahlung imaging. While high-energy photons are created near the decay site, most low-energy bremsstrahlung photons are produced farther from the $^{90}Y$ decay location (*26*). On the other hand, degradation of the bremsstrahlung image is, in part, due to septal penetration from high-energy photons of the continuous-energy spectrum from $^{90}Y$ decay. These photons are accepted in the selected energy window as Compton scattered events in the camera crystal. The energy distribution of these scattered photons within the selected energy window influences image resolution. The choice of collimation and energy window represents a practical compromise between sensitivity and spatial resolution requirements for specific circumstances. A systematic study of the choice of collimation and energy window for $^{90}Y$ was conducted to achieve optimal image quality under practical clinical conditions. Acquisition parameters and quantitation methods were also evaluated under realistic clinical conditions using a patient phantom. Our study showed that degradation in spatial resolution with increase in energy-window width was small for the bremsstrahlung continuous energy spectrum (Table 3), while sensitivity was more than 70% greater for a 50–290-keV window when compared to a 50–150-keV window with the ME collimator (Table 2). Spatial resolution was greatly decreased because of registration of penetrating photons when energy windows beyond the manufacturer's specifications for the collimator were used. For example, FWHM was 30 mm for a 144–176-keV energy window when compared to 15 mm for a 50–150-keV energy window using the LEAP collimator. Therefore, the selection of a broad-energy window so there is more than 95% energy collimation is preferable. When we used a ME collimator and an energy window of 55–285 keV, about 30 min was required to record a total of one-

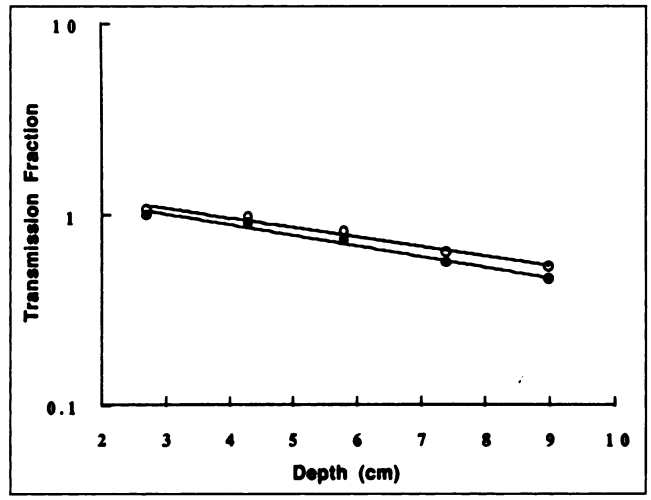


**FIGURE 5.** Transmission fraction measurements for a 5-cm diameter spherical source at various depths in water. The source ROIs were defined as the actual source size (○-○) and twice the actual source size (●-●). The correlation coefficients of the regression fitting was 0.99 for each ROI. A single effective $\mu$ value can be used for attenuation correction even with multi-energy photon flux acquired in a broad energy window.

**TABLE 6**
Average Attenuation Coefficient Values ($\mu$) for a Narrow-Beam Yttrium-90 Source Transmitted Through Scattering Medium (Lucite, density = 0.944 g/cc)

| Collimator | Energy window (keV) | $\mu$ ($cm^{-1}$) |
|---|---|---|
| Low-energy | 68–83 | 0.176 |
| | 50–150 | 0.172 |
| Medium-energy | 68–83 | 0.173 |
| | 55–285 | 0.168 |

**TABLE 7**
Accuracy of Yttrium-90 Activity Estimation in an Alderson Abdominal Phantom

| Organ/Tumor | Method* | Actual activity MBq ($\mu$Ci) | Estimated activity MBq ($\mu$Ci) | Error† (%) |
|---|---|---|---|---|
| Liver | GM/ACF | 98.8 (2670) | 86.9 (2350) | −12 |
| Spleen | EPS/$\mu$ | 17.0 (460) | 15.8 (428) | −7 |
| 4-cm tumor | GM/$\mu$ | 6.66 (180) | 6.59 (178) | −1 |
| 2-cm tumor | EPS/$\mu$ | 1.85 (50.0) | 1.63 (44.0) | −13 |

*The geometric-mean method was used to estimate activity in the liver and 4-cm tumor seen in conjugate views (anterior and posterior). The effective point-source method was used to estimate activity in the spleen and 2-cm tumor clearly seen in only a single view. Photon attenuation was corrected using a transmission scan ACF or a $\mu$ value of 0.131 $cm^{-1}$.

†Underestimation of activity in organ or tumor is indicated by the negative value of the activity estimation error.

million counts in a single static view of a patient with total-body activity of 148 MBq (4 mCi) of $^{90}$Y. This corresponds to the case of imaging at day 4 during the imaging sequence after administration of 555 MBq (15 mCi) of $^{90}$Y labeled antibodies (*2*). There was greater sensitivity when the LEAP collimator was used but image degradation was severe with poor system resolution and signal-to-noise ratio (Table 5). Although spatial resolution and signal-to-noise ratio of the ME collimator were slightly lower than that of the HE collimator (Table 5), sensitivity of the ME collimator was almost two times greater than that of the HE collimator, thereby confirming the advantage of the ME collimator for clinical circumstances.

Quantitation of radionuclide content in organs and tumors depends upon accurate correction for photon attenuation. The influence of source ROI size on the linear attenuation coefficient ($\mu$) was not great. The correlation coefficient of the regression fit for transmission fraction and source depth was 0.99, despite the multi-energy bremsstrahlung photon flux and the spatial dependence of the continuous spectrum. The broad photon beam radiating from the transmission source was suitable for attenuation correction for large source objects containing $^{90}$Y, as has also been reported for single-photon emitters (*7,8*). However, increased scattering in bremsstrahlung imaging made the ACF value more sensitive to photon-beam geometry than observed for $^{131}$I. For $^{131}$I, the ACF reported for a 4-cm tumor using transmission imaging was 2.50, whereas that using transmission fraction data was 3.18 (*27*). On the other hand, for $^{90}$Y, the ACF for a 4-cm tumor using transmission imaging or transmission fraction data was found to be 1.40 and 4.11, respectively.

Because of cross-talk between adjacent source objects, the visual boundaries of the organ and tumor on images were less definite when compared to those from a photopeak emitting radionuclide such as $^{131}$I. Organ and tumor ROI definition was more difficult, leading to erroneous activity quantitation. This problem was overcome by subtracting background activity. With appropriate attenuation correction and background subtraction, the quantitation errors for organs and tumors were less than 15% and were comparable to the quantitation errors observed for $^{131}$I (*10*). Variation in background ROI selection had more influence on quantitation of a small-source object than on a large-source object. A background ROI appropriate for the body thickness of the organ or tumor ROI was easily selected in the abdominal phantom because background activity was uniformly distributed. Background subtraction is more complicated in patients because background can be distributed less uniformly but can be managed using a systematic approach to background selection (*7,8*). Organ and tumor edge detection can be improved using a restoration filter for resolution recovery; results from this investigation will be included in a separate study (*28*).

## ACKNOWLEDGMENTS

The authors thank Cathy Suey, CNMT, for technical assistance. This research was supported by grants from the Department of Energy (DE-FG03-84ER60233) and the National Cancer Institute (PHS CA 47829).

## REFERENCES

1. Stewart JSW, Hird V, Snook D et al. Intraperitoneal iodine-131- and yttrium-90-labeled monoclonal antibodies for ovarian cancer: pharmacokinetics and normal tissue dosimetry. *Int J Cancer Suppl* 1988;3:71.
2. DeNardo SJ, Kramer EL, Richman CM et al. Radioimmunotherapy of breast cancer with yttrium-90/Indium-111 BRE-3 current clinic results and therapeutic potential. *J Nucl Med* 1993;34:53.
3. Hnatowich DJ, Virzi F, Doherty PW. DTPA-coupled antibodies labeled with yttrium-90. *J Nucl Med* 1985;26:503–509.
4. DeNardo GL, Kroger LA, DeNardo SJ et al. Comparative toxicity studies of yttrium-90 MX-DTPA and 2-IT BAD conjugated monoclonal antibody (BrE-3). *Cancer* 1993;73:1012–1022.
5. Siegel JA, Handy DM, Kopher KA, Zeiger LS, Order SE. Therapeutic beta irradiating isotopes in bone metastasis: a technique for bremsstrahlung imaging and quantitation. *Antib Immunoconjug Radiopharm* 1992;5:237–248.
6. Clarke LP, Cullom SJ, Shaw R et al. Bremsstrahlung imaging using the gamma camera: factors affecting attenuation. *J Nucl Med* 1992;33:161–166.
7. DeNardo GL, DeNardo SJ, Macey DJ, Mills SL. Quantitative pharmacokinetics of radiolabeled monoclonal antibodies for imaging and therapy in patients. In: Srivastava SC, ed. *Radiolabeled monoclonal antibodies for imaging and therapy*. New York: Plenum Publishing Co.; 1988:293–310.
8. Macey DJ, DeNardo GL, DeNardo SJ. A treatment planning program for radioimmunotherapy. In: Vaeth JM, ed. *Frontiers of radiation therapy and oncology*. Basel: Karger; 1990:123–131.
9. Thomas SR, Maxon HR, Kereiakes JG. In vivo quantitation of lesion radioactivity using external counting methods. *Med Phys* 1976;3:253–255.

10. Hammond ND, Moldofsky PJ, Beardsley MR, Nulhern CB. External imaging techniques for quantitation of distribution of Iodine-131 F(ab')2 fragments of monoclonal antibody in humans. *Med Phys* 1984;11:778–783.
11. Leichner PK, Yang NC, Frenkel TL. Dosimetry and treatment planning for yttrium-90-labeled antiferritin in hepatoma. *Intl J Radiat Oncol Biol Phys* 1987;14:1033–1042.
12. Parker BA, Vassos A, Halpern SE, et al. Yttrium-90-anti-idiotype therapy on non-Hodgkin's lymphoma. *Cancer Res* 1990;50:1022s–1028s.
13. Robinson RG, Spicer JA, Preston DE, Wegst DE, Martin NL. Treatment of metastatic bone pain with strontium-89. *Nucl Med Biol* 1987;14:219–222.
14. Silberstein EB, Williams C. Strontium-89 therapy for the pain of osseous metastases. *J Nucl Med* 1985;26:345–348.
15. Tenvail J, Darte L, Lundgren R, El Hassan AM. Palliation of multiple bone metastases from prostatic carcinoma with strontium-89. *Acta Oncol* 1988; 27:365–369.
16. Vriesendorp HM, Herpst JM, Leichner PK, Klein JL, Order SE. Polyclonal yttrium-90-labeled antiferritin for refractory Hodgkin's disease. *Int J Radiat Oncol Biol Phys* 1989;17:815–821.
17. Blake GM, Zivanovic MA, Blaquiere RM, Fine DR, McFwan AJ, Ackery DM. Strontium-89 therapy: measurement of adsorbed dose to skeletal metastases. *J Nucl Med* 1988;29:549–557.
18. Buchali K, Correns HJ, Schuerer M, Schnorr D, Lips H, Sydow K. Results of a double blind study of $^{89}$St-therapy of skeletal metastases of prostatic carcinoma. *Eur J Nucl Med* 1988;14:349–351.
19. Correns HJ, Mebel M, Buchali K, Schnorr D, Scidel C, Mitterlaechner E. Strontium-89 therapy of bone metastases of carcinoma of the prostate gland. *Eur J Nucl Med* 1979;4:33–35.
20. Deshpande SV, DeNardo SJ, Kukis DL et al. Yttrium-90-labeled monoclonal antibody for therapy: labeling by a new macrocyclic bifunctional chelating agent. *J Nucl Med* 1990;31:473–479.
21. Kyle V, Hazelman BL, Wraight EP. Yttrium-90 therapy and $^{99m}$Tc pertechnetate knee uptake measurements in the management of rheumatoid arthritis. *Ann Rheum Dis* 1983;42:132–137.
22. Boye E, Lindegaard MW, Paus E, Sketting A, Davy M, Jakobsen E. Whole-body distribution of radioactivity after intraperitoneal administration of $^{32}$P colloids. *Br J Radiol* 1984;57:395–402.
23. Ott RL, Flower MA, Jones A, McReady VR. The measurement of radiation doses from $^{32}$P chromic phosphate therapy of the peritoneum using SPECT. *Eur J Nucl Med* 1985;11:304–308.
24. Balanchandran S, McGuire L, Flanigan S, Shah H, Boyd CM. Bremsstrahlung imaging after $^{32}$P treatment for suprasellar cyst. *Int J Nucl Med Biol* 1985;12:215–221.
25. Smith T, Crawley JCW, Shawe DJ, Gumpel JM. SPECT using bremsstrahlung to quantify yttrium-90 uptake in Baker's cysts: its application in radiation synovectomy of the knee. *Eur J Nucl Med* 1988;14:498–503.
26. Simpkin DJ, Cullom SJ, Mackie TR. The spatial and energy dependence of bremsstrahlung production about beta point sources in $H_2O$. *Med Phys* 1992;19:105–114.
27. DeNardo GL, Shen S, DeNardo SJ, Liao SK, Yu S, Macey DJ. Validation of nuclear quantitation of tumor size and Iodine-131 amount in an Alderson phantom by planar imaging. *J Nucl Med* 1992;33:128.
28. Shen S, DeNardo GL, DeNardo SJ. Quantitative bremsstrahlung imaging of $^{90}$Y using a Wiener filter. *Med Phys* 1994: in press.